Supplementary Information (SI) for Journal of Materials Chemistry A.
This journal is © The Royal Society of Chemistry 2026

Gradient Inverse Temperature Crystallization for High-Quality $MAPbBr_3$ Perovskite Single Crystals and Supreme-Sensitivity X-ray Detectors

Shuo-Hua Han, [†a] Lu-Di Zhang, [†a] Yu-Cheng Liu, *[b] Hong-Jian Feng*[a]

[a] School of Physics, Northwest University, Xi'an 710127, P. R. China.

[b] School of Materials Science and Engineering, Shaanxi Normal University, Xi'an 710119, P. R. China.

* Corresponding authors. E-mail addresses: hjfeng@nwu.edu.cn (Hong-Jian Feng), liuyc@snnu.edu.cn (Yu-Cheng Liu).

[†] Equal contribution.

Experimental Section

Chemicals and Reagents: Lead bromide ($PbBr_2$, 99.0%) and N,N-Dimethylformamide (DMF, ≥99.8%) were purchased from Aladdin Reagent Ltd., China. Methylamine Hydrobromide (MABr, 99.5%) were purchased from Xi'an yuri Solar Co., Ltd. . High-purity gold electrode material was purchased from a commercial source. All the chemicals were used as received without further purification.

Growth of Perovskite Single Crystals: A $MAPbBr_3$ precursor solution with a stoichiometric molar ratio of 1.2:1 was prepared by dissolving 0.671 g of methylammonium bromide (MABr, 6 mmol) and 1.834 g of lead bromide ($PbBr_2$, 5.0 mmol) in 4 mL of N,N-dimethylformamide (DMF) solvent. The solution was magnetically stirred at room temperature (≈25°C) for 1 hour and subsequently filtered through a 0.22 μm PTFE filter into a 40 mm × 35 mm glass container. Subsequently, the glass container was placed in an oil bath for heating. After the solution has been cooled to room temperature, the crystal can be retrieved.

Device Fabrication: Under vacuum conditions, gold electrodes with a thickness of 100 nm were deposited on both sides of the $MAPbBr_3$ single crystal to fabricate a sandwich-structured device. The electrode area was 4 mm^2. One electrode was affixed to a gold-

coated substrate using carbon paste, while the other electrode was connected to a gold wire using carbon paste.

Characterizations: The surface morphology of $MAPbBr_3$ samples was characterized using a Thermo Scientific Apreo S scanning electron microscope (SEM). X-ray diffraction (XRD) 2θ scans of $MAPbBr_3$ were performed using a Bruker D8 Advance. The target source is Cu, with a wavelength of 1.540598 Å. High-resolution XRD rocking curves and phi scans of the $MAPbBr_3$ single crystal were measured using an X'Pert Pro MRD. The ultraviolet-visible (UV-Vis) absorption spectrum of the $MAPbBr_3$ single crystal was obtained using a UV-3600 spectrophotometer equipped with an integrating sphere accessory. The steady-state photoluminescence (PL) and time-resolved photoluminescence (TRPL) of $MAPbBr_3$ single crystals were investigated using an Edinburgh FLS1000. For the time-resolved photoluminescence (TRPL) test, the excitation wavelength was set to 330 nm, the emission wavelength was 544 nm, the slits were set to 2 during the test, and the initial photon count rate was adjusted to 3000 cps.

X-ray Detector Characterization: To reduce electromagnetic interference and the impact of ambient light, we measured the X-ray detection performance of the SC detector in a homemade lead box. The X-ray source used was an X-ray tube equipped with a tungsten target (Spellman, XRB150PN600), with an acceleration voltage of 45 kV. The tube current was adjusted between 1 and 4 mA to achieve the desired X-ray dose rate. To further reduce the X-ray dose rate, a 3 mm thick aluminum plate was used as an attenuator between the X-ray source and the detector. Prior to the measurement, the X-ray dose rate was precisely calibrated using a Fluke silicon diode dosimeter (RaySafe X2). A precision source meter (FS380) was used to provide an electric field for the detector, and the X-ray response current was recorded.

The time-resolved photoluminescence was fitted using a double exponential decay function. The specific formula is as follows:

$$I(t) = A_1 exp\left(-t/\tau_1\right) + A_2 exp(-t/\tau_2)$$

where $I(t)$ is the photoluminescence intensity at time t; τ_1 and τ_2 represent the time constants for the fast and slow decay components, respectively; and A_1 and A_2 are the corresponding fractional amplitude coefficients.

Average lifetime (τ_{ave}) formula:

$$\tau_{ave} = \frac{A_1\tau_1^2 + A_2\tau_2^2}{A_1\tau_1 + A_2\tau_2}$$

The relationship between the trap density and VTFL was described by the following formula:

$$n_{trap} = \frac{2\varepsilon_0\varepsilon V_{TFL}}{qL^2}$$

where εo is the vacuum permittivity, q and L are the elementary charge and crystal thickness, respectively, and ε is the dielectric constant of the perovskite SC (25.5)[1].

The data is fitted using the modified Hecht equation to obtain the μτ product, with the formula as follows:

$$I = \frac{I_0\mu\tau V}{L^2}\frac{1 - exp(-\frac{L^2}{\mu\tau V})}{1 + \frac{LS}{V\mu}}$$

where I_0 is the saturation photocurrent, and L and V are the thickness of the single crystal and the applied voltage, respectively.

The sensitivity calculation formula for X-ray detectors:

$$S = \frac{J_p - J_d}{A \times D}$$

In the formula, J_p and J_d represent the X-ray-induced photocurrent and the dark current, respectively, A denotes the effective surface area under X-ray irradiation, and D stands for the X-ray dose rate.

The formula for calculating the signal-to-noise ratio:

$$SNR = \frac{I_{signal}}{I_{noise}}$$

In this formula, I_{signal} represents the signal current (its value is the average photocurrent minus the average dark current), and I_{noise} denotes the noise current.

$$I_{noise} = \sqrt{\frac{1}{N}\sum_{i}^{N}(I_i - \bar{I}_p)^2}$$

Details of DFT calculations for intrinsic defects in $MAPbBr_3$ materials：

All first-principles calculations in this study were conducted based on density functional theory (DFT) using the PWmat software package.[2, 3] To systematically investigate defect properties, a 2×2×2 supercell model was constructed, and twelve possible intrinsic point defects in $MAPbBr_3$ were comprehensively examined, including three vacancy defects (V_{MA}, V_{Pb}, V_{Br}), three interstitial defects (MA_i, Pb_i, Br_i), and six substitutional defects (MA_{Pb}, Pb_{MA}, MA_{Br}, Pb_{Br}, Br_{MA}, Br_{Pb}). Structural optimization was performed using the GGA-PBE functional, with a plane-wave cutoff energy of 680 eV, a k-point mesh of 2×2×2, and a convergence criterion set to a maximum atomic force of less than 0.02 eV/Å. Self-consistent calculations were further carried out with the HSE06 hybrid functional to enhance the accuracy of electronic structure descriptions.

Under thermodynamic equilibrium growth conditions, the existence of $MAPbBr_3$ must satisfy:

$$\mu_{CH_3NH_3} + \mu_{Pb} + 3\mu_{Br} = \Delta H(CH_3NH_3PbBr_3) = -6.60\ eV,$$

where μ_i denotes the chemical potential of constituent element i relative to its most stable phase, and $\Delta H(CH_3NH_3PbBr_3)$ represents the formation enthalpy of MAPbBr3. For the chemical potential of the CH_3NH_3 group, the body-centered cubic (bcc) structure of CH_3NH_3 is adopted as the reference phase, following the structural selection scheme used for Cs.[4, 5] To prevent the formation of competing phases such as $PbBr_2$ and rock-salt structured CH_3NH_3Br, the following additional constraints must be satisfied:

$$\mu_{CH_3NH_3} + \mu_{Br} < \Delta H(CH_3NH_3Br) = -3.89\ eV,$$

$\mu_{Pb} + 2\mu_{Br} < \Delta(PbBr_2) = -2.60\ eV$.

The defect formation energy was calculated using the following formula[6-9]:

$$E(X) = E_{total}(X) - E_{bulk} + \sum_i n_i\mu_i + qE_F + E_{corr}$$

where $E_{total}(X)$ represents the total energy of the defective system, E_{bulk} denotes the total energy of the defect-free bulk system, μ_i represents the atomic chemical potential, q indicates the net charge of the system, $E_F=\varepsilon+E_{VBM}$ corresponds to the external electron chemical potential, and E_{coor} denotes the energy correction for finite-size and mirror charge effects. It should be noted that charging of the defect was achieved by adjusting the total number of electrons within the framework of the gel model.

Transition Level Formula:

$$\epsilon(q_1/q_2) = \frac{E^f\left(X^{q_1};E_F=0\right) - E^f(X^{q_2};E_F=0)}{q_2 - q_1}$$

Where $E^f\left(X^q;E_F=0\right)$ represents the formation energy of defect X in charge state q when the Fermi level is at the valence band maximum ($E_F = 0$).

Detailed Comparative Analysis Between $MAPbBr_3$ and $CsPbBr_3$:

From the intrinsic properties of the material, the presence of organic methylammonium (MA^+) cations in $MAPbBr_3$ significantly enhances the dynamic flexibility and overall stability of the crystal lattice.[10] The inorganic lead-bromide octahedral framework is stabilized by MA^+ cations via hydrogen bonding, which endows $MAPbBr_3$ with strong defect tolerance and facilitates the relaxation of lattice strain during the crystallization process.[11] Therefore, the intrinsic defect density of $MAPbBr_3$ single crystals is inherently 1–2 orders of magnitude lower than that of inorganic $CsPbBr_3$ single crystals.[12, 13] Excellent carrier transport characteristics and charge collection efficiency are endowed to $MAPbBr_3$ single crystals by its lower intrinsic defect density and higher carrier mobility-lifetime ($\mu\tau$) product. An ultrahigh detection sensitivity at the level of hundreds of thousands is finally achieved. In sharp

contrast, the sensitivity of state-of-the-art $CsPbBr_3$ detectors is currently limited to the level of tens of thousands.[14, 15]

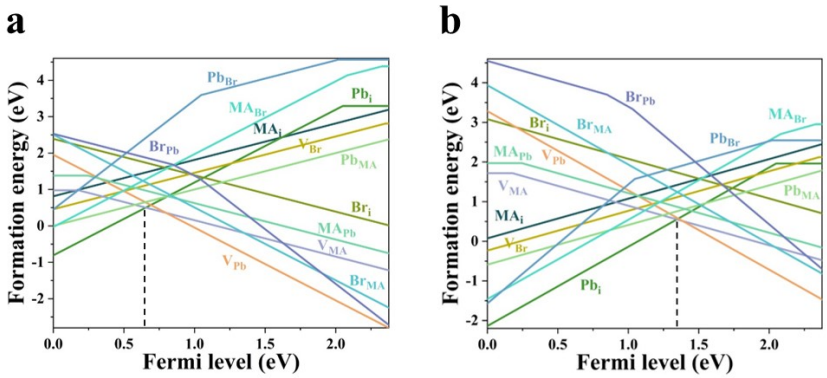

Figure S1. The formation energies of intrinsic point defects in $MAPbBr_3$ at different chemical potential points: (a) Moderate, (b) Bromine-poor/lead-rich.

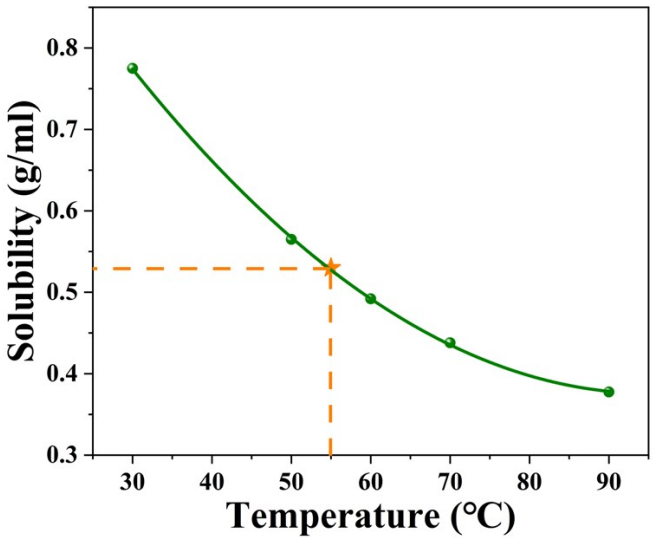

Figure S2. Temperature-dependent solubility curve of $MAPbBr_3$ in DMF.

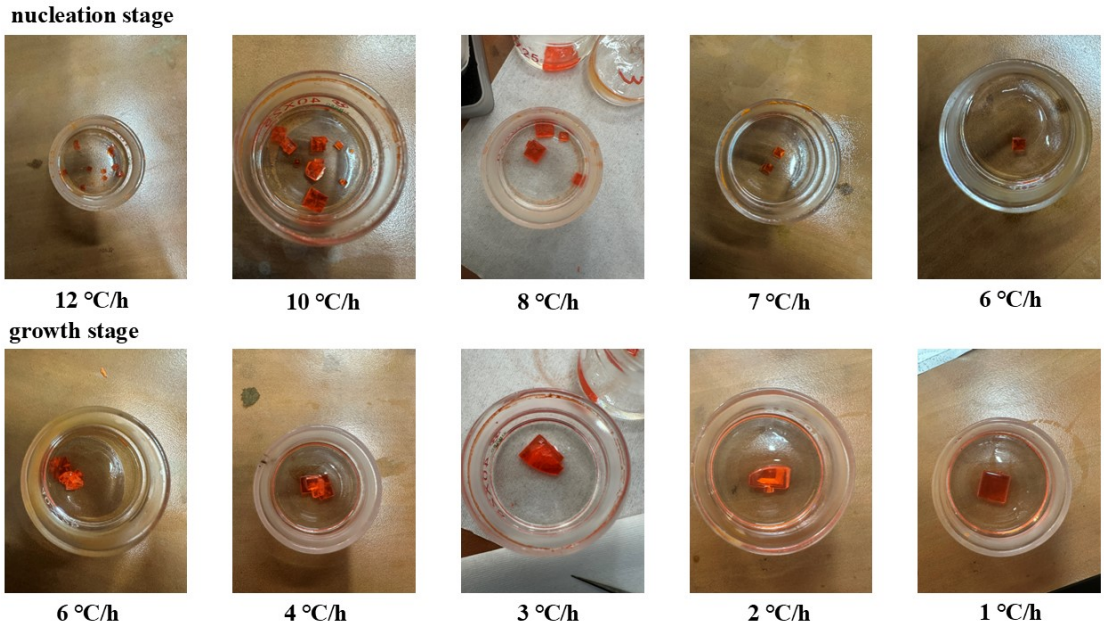

Figure S3. Photographs of single crystals grown at different heating rates during the nucleation and growth stages.

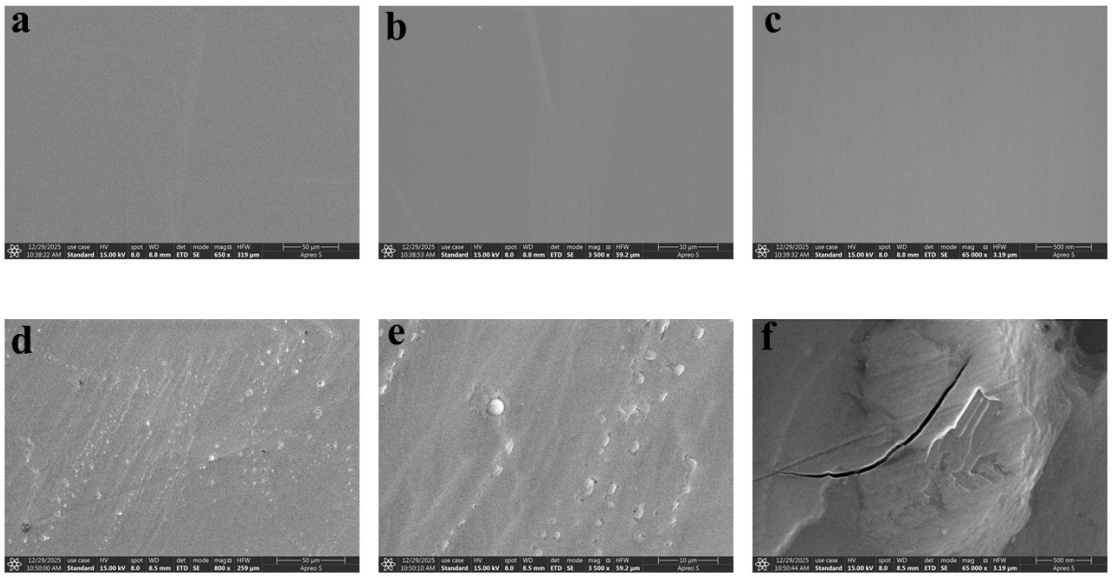

Figure S4. (a), (b), (c) are SEM images of the G-ITC SC under different scale bars; (d), (e), (f) are SEM images of the ITC SC under different scale bars.

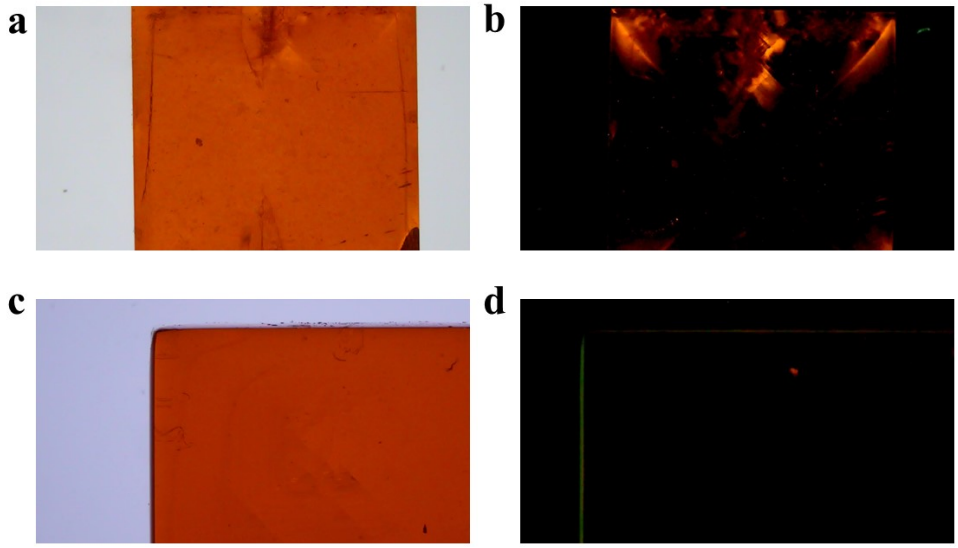

Figure S5. Micrographs of single crystals grown by different methods. (a),(b): Conventional and cross-polarized micrographs of ITC-grown SC. (c),(d): Conventional and cross-polarized micrographs of G-ITC-grown SC.

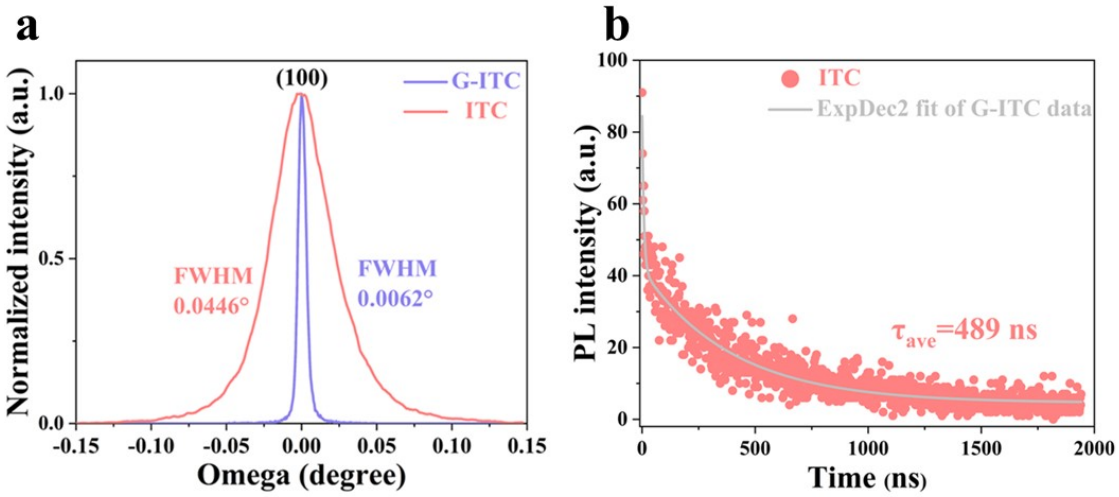

Figure S6. (a) High-resolution XRD rocking curves of the (100) diffraction peak of $MAPbBr_3$ SCs grown by the G-ITC and ITC methods. (b) Time-Resolved Photoluminescence of $MAPbBr_3$ SCs grown by ITC method.

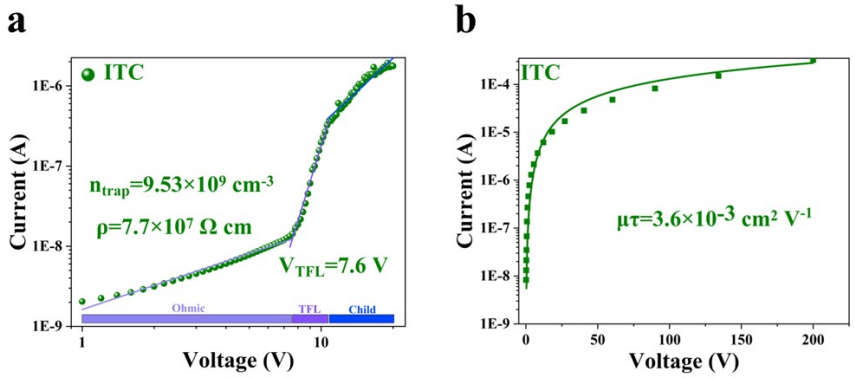

Figure S7. (a) Measurement of trap density and resistivity in SCs grown by ITC method using the Space-Charge-Limited Current (SCLC) method. (b) Bias Voltage-Dependent Photoconductivity Measurements of Single Crystals Grown by the ITC Method.

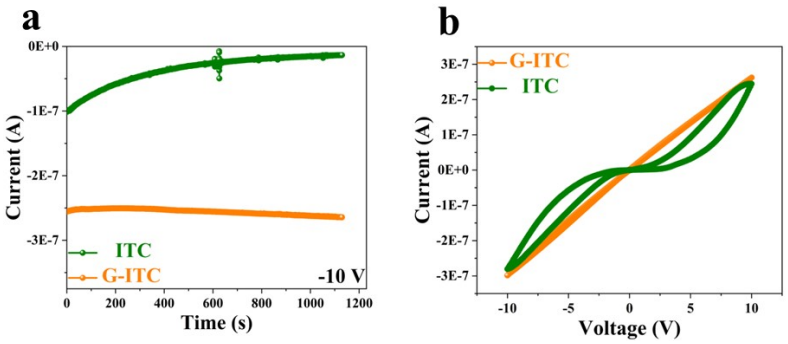

Figure S8. Dark current characteristics of ITC and G-ITC fabricated $MAPbBr_3$ SC devices. (a) Current-time curves under -10 V constant bias; (b) Cyclic I-V curves from -10 V to 10 V.

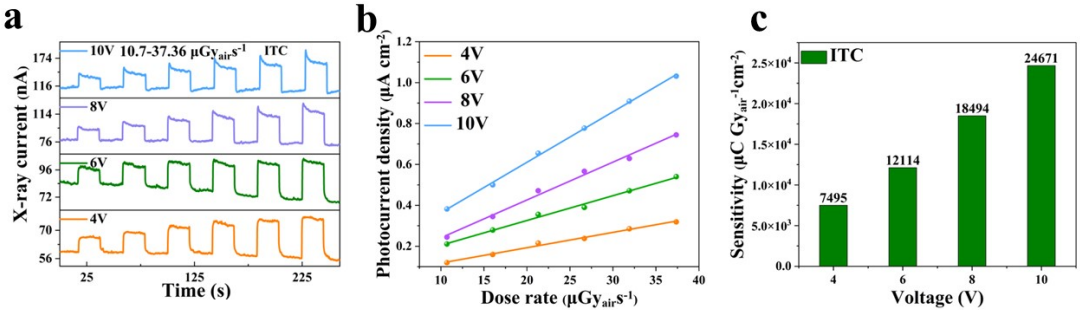

Figure S9. X-ray detectors fabricated from $MAPbBr_3$ single crystals grown by the ITC method. (a) X-ray response current at different bias voltages and dose rates. (b) Graph of the variation of X-ray photocurrent density with dose rate under different external biases. (c) Sensitivity of X-ray devices within a bias range of 4-10V.

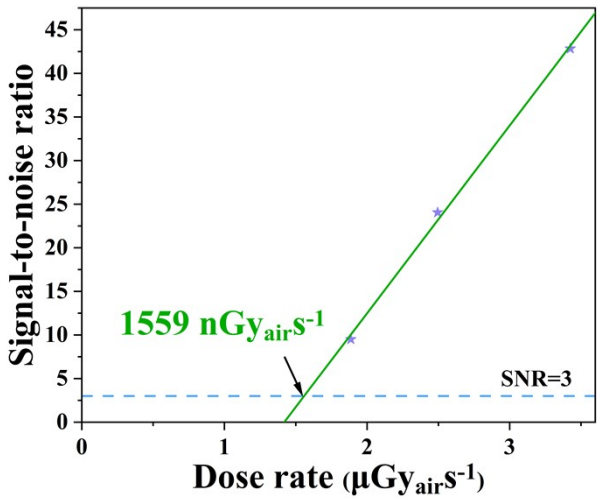

Figure S10. Signal-to-noise ratio (SNR) of the detector fabricated from single crystals grown by the ITC method.

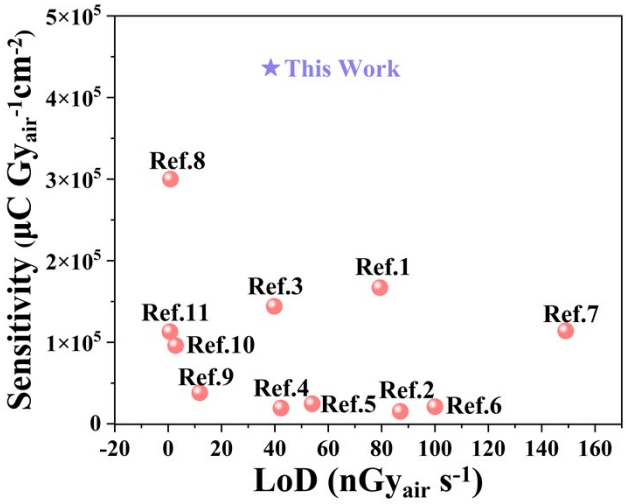

Figure S11. Comparison of sensitivity and low detection limit for X-ray detectors based on $MAPbBr_3$ SCs grown by different methods.

Table S1. Detailed TRPL fitting parameters for $MAPbBr_3$ single crystals grown by G-ITC and ITC methods.

	A_1	τ_1(ns)	A_2	τ_2(ns)	τ_{ave}(ns)
G-ITC	5530.90	1888.46	1676.48	4823.09	3169
ITC	19.25	79.69	30.10	528.88	489

Table S2. A Summary of the Characterization of $MAPbBr_3$ SCs and the Optoelectronic Performance of X-ray Detectors Fabricated Therefrom.

Ref.	Methods	FWHM of rocking curve (°)	PL peak (nm)	τ (ns)	n_{trap} ($\times10^9$ cm^{-3})	Electrical resistivity (Ω cm)	μτ ($\times10^{-2}$ cm^2 V^{-1})	LoD ($nGy_{air}s^{-1}$)	Sensitivity (μC $Gy_{air}^{-1}cm^{-2}$)
1	SS-ITC	0.0346	——	1658	7.93	——	1.73	79.33	1.67×10^5
16	LDSC	0.0096	540	1099	4.5	——	1.495	——	2181
17	Laser-assisted	——	538	1380	190	——	——	39.8	1.44×10^5
18	LTGC	0.0190	547	815	6.7	——	——	——	——
19	VEC	0.0092	551	1150	2.280	——	——	54	24552
20	Si-integrated	——	——	692	1-10	——	——	<100	2.1×10^4
21	Low-temperature hot-pressing	——	——	——	3.040	2.08×10^7	0.782	149	1.14×10^5
22	Silicone-Assisted	0.0052	——	——	0.215	——	0.11	0.85	3×10^5
23	ITC.1	——	559	——	——	——	——	11.84	3.81×10^4
24	ITC.2	——	——	——	——	——	——	2.8	96000
25	ITC.3	0.0140	542	22.2	——	——	——	0.7	1.13×10^5
26	ITC.4	0.0080	533	39.89	——	8.28×10^7	——	87	15280
27	PTG	0.0080	538	1002	4.250	——	——	670	7275
28	With CF3-PABr	0.0090	——	85	23.20	——	6.0	1.3	1.088×10^5
29	CSG	——	——	——	0.822	——	0.33	15.7	2.35×10^5
30	ITC.5	0.0128	540	176	6.290	——	0.142	17.8	5.4×10^4
31	ITC.6	——	576.6	63	0.945	8.82×10^7	1.6	42.3	19370
This work	ITC	0.0428	549	489	9.530	7.7×10^7	0.36	1559	24671
This work	G-ITC	0.0055	549	3169	0.473	5.8×10^7	1.6	38.5	4.36×10^5

References

1. F. Yu, Y. Song, L. Wang, Y. Yang, J. Wang, X. Shen, B. Jin, H. Song, Y. Fang and Q. Dong, *Small*, 2025, **21**, 2407109.
2. W. Jia, Z. Cao, L. Wang, J. Fu, X. Chi, W. Gao and L.-W. Wang, *Computer Physics Communications*, 2013, **184**, 9-18.

3. W. Jia, J. Fu, Z. Cao, L. Wang, X. Chi, W. Gao and L.-W. Wang, *Journal of Computational Physics*, 2013, **251**, 102-115.
4. T. Shi, W.-J. Yin, F. Hong, K. Zhu and Y. Yan, *Applied Physics Letters*, 2015, **106**.
5. W.-J. Yin, T. Shi and Y. Yan, *Applied physics letters*, 2014, **104**.
6. C. Freysoldt, B. Grabowski, T. Hickel, J. Neugebauer, G. Kresse, A. Janotti and C. G. Van de Walle, *Reviews of modern physics*, 2014, **86**, 253-305.
7. Z.-J. Suo, J.-W. Luo, S.-S. Li and L.-W. Wang, *Physical Review B*, 2020, **102**, 174110.
8. J. Xiao, K. Yang, D. Guo, T. Shen, H.-X. Deng, S.-S. Li, J.-W. Luo and S.-H. Wei, *Physical Review B*, 2020, **101**, 165306.
9. J.-H. Yang, W.-J. Yin, J.-S. Park and S.-H. Wei, *Scientific reports*, 2015, **5**, 16977.
10. T. Yin, Y. Fang, X. Fan, B. Zhang, J.-L. Kuo, T. J. White, G. M. Chow, J. Yan and Z. X. Shen, *Chemistry of Materials*, 2017, **29**, 5974-5981.
11. X. Ma, X. Tian, E. Stippell, O. V. Prezhdo, R. Long and W.-H. Fang, *Journal of the American Chemical Society*, 2024, **146**, 29255-29265.
12. R. Zha, L. He, T. Shi and M. Zhang, *Advanced Composites Hybrid Materials*, 2026.
13. W. Jia, Y. Li, Y. Liu, Z. Wei, S. Liu, C. Liu, D. C. Onwudiwe, B. S. Bae, Y. Zhou and X. Xu, *ACS Photonics*, 2025, **13**, 163-174.
14. A. G. Benadia, L. Pan, K. S. Bayikadi, Z. Liu, J. A. Peters, G. J. Snyder, M. G. Kanatzidis and Design, *Crystal Growth Design*, 2025, **25**, 9288-9299.
15. X. Sun, G. Zhang, W. Ma, Y. Hua, H. Liu, J. Liu, Z. Yue, X. Wang, J. Song and X. Tao, *Advanced Materials*, 2026, **38**, e12788.
16. Z. Zhang, H. Li, H. Di, D. Liu, W. Jiang, J. Ren, Z. Fan, F. Liao, L. Lei and G. Li, *ACS Applied Electronic Materials*, 2022, **5**, 388-396.
17. S. Liu, Y. Ding, X. Wang, Y. Li, J. Chen, Z. Zhao, Z. Zhu, J. Wu, O. E. Fayemi and B. S. Bae, *Advanced Electronic Materials*, 2024, **10**, 2300555.
18. Y. Liu, Y. Zhang, Z. Yang, J. Feng, Z. Xu, Q. Li, M. Hu, H. Ye, X. Zhang and M. Liu, *Materials Today*, 2019, **22**, 67-75.
19. D. Liu, X. Sun, L. Jiang, X. Jiang, H. Chen, F. Cui, G. Zhang, Y. Wang, Y.-B. Lu and Z. Wu, *Journal of Materials Chemistry A*, 2024, **12**, 12467-12474.
20. W. Wei, Y. Zhang, Q. Xu, H. Wei, Y. Fang, Q. Wang, Y. Deng, T. Li, A. Gruverman and L. Cao, *Nature Photonics*, 2017, **11**, 315-321.
21. W. Tan, Y. Xiao, C. Zhou, X. Jin, S. Zhu, M. Han, Z. Tang, Y. Zhang, Z. Su and T. Chen, *Advanced Functional Materials*, 2024, **34**, 2406839.
22. L. Wang, Y. Yan, M. Bu, J. Wang, L. Li, Y. Li, H. Liu, H. Zhang, X. Pi and D. Yang, *Advanced Functional Materials*, 2025, **35**, 2415378.
23. N. He, L. Zhang, X. He, J. Guo, X. Wu, Q. Li and J. He, *Advanced Optical Materials*, 2024, **12**, 2400707.
24. W. Zhang, H. Wang, Z. Chen, P. Wang, X. Liu, H. Dong, J. Zhao, Y. Cui and Y. Shao, *ACS Applied Materials Interfaces*, 2024, **16**, 12844-12852.

25. P. Wang, H. Wang, J. Fu, H. Dong, W. Zhang, Z. Gao and Y. Shao, *ACS Photonics*, 2024, **11**, 5409-5417.
26. L. Chen, H. Wang, W. Zhang, F. Li, Z. Wang, X. Wang, Y. Shao and J. Shao, *ACS Applied Materials Interfaces*, 2022, **14**, 10917-10926.
27. D. Liu, L. Jiang, X. Jiang, X. Sun, G. Zhang, Y.-B. Lu, Y. Wang, Z. Wu and Z. Ling, *ACS Applied Materials Interfaces*, 2023, **15**, 57846-57855.
28. Z. Chen, H. Wang, J. Fu, P. Wang, X. Liu, H. Dong, S. Yang and Y. Shao, *Journal of Materials Chemistry A*, 2024, **12**, 14446-14455.
29. Q. Xu, A. Datta, K. Becla, P. Becla and S. Motakef, *Chemical Engineering Journal*, 2023, **475**, 146155.
30. M. Hu, Y. Chen, P. Tan, J. Liu, T. Liu, M. Sun, L. Huang, L. Cheng, X. Ma and S. Yu, *IEEE Electron Device Letters*, 2025.
31. M. Han, Y. Xiao, C. Zhou, Z. Xiao, W. Tan, G. Yao, X. Wu, R. Zhuang, S. Deng and Q. Hu, *Advanced Functional Materials*, 2023, **33**, 2303376.